ADVANCED ENERGY MATERIALS
www.advenergymat.d

Molecular Engineering of Organic Spacer Cations for Efficient and Stable Formamidinium Perovskite Solar Cell

*Sungwon Song, Seok Joo Yang, Wookjin Choi, Hansol Lee, Woong Sung, Chaneui Park, and Kilwon Cho**

Low dimensional (LD) perovskite materials generally exhibit superior chemical stability against ambient moisture and thermal stress than that of 3D perovskites. Recently, LD perovskite has been used as a passivation layer on the surface of 3D perovskite grains. Although various LD perovskites have been developed focusing on their hydrophobicity, the impact of crystal structure of LD perovskite on the photovoltaic performance of perovskite solar cell (PSC) is still uncertain. In this work, the effects of the structural characteristics of LD perovskites on the crystal formation of formamidinium lead triiodide (α-FAPbI$_3$) and on the optoelectrical properties of PSCs are elucidated. The phase-transformation kinetics of FAPbI$_3$ mixed with LD perovskites is studied using the Johnson–Mehl–Avrami–Kolmogorov model. It is found that the arrangement of PbI$_6$ octahedra in the LD perovskite changes the rate of α-FAPbI$_3$ formation. Facilitated nucleation of α-FAPbI$_3$ at the LD/FAPbI$_3$ interface results in minimal structural disorder and prolonged charge-carrier lifetimes. As a result, the PSC with the optimized LD perovskite structure exhibits a power conversion efficiency of 21.25% from a reverse current–voltage scan, and stabilized efficiency of 19.95% with excellent ambient stability without being encapsulated.

1. Introduction

Metal halide perovskites have a large light-absorption coefficient and long carrier-diffusion length.[1] Excellent optoelectronic properties make them attractive for use in photovoltaic devices.[2–4] Among various perovskite materials, formamidinium lead triiodide (α-FAPbI$_3$)-based perovskites, which exhibit a narrow bandgap and excellent charge-transport properties, have achieved a certified power conversion efficiency (PCE) of 25.2% in 2019.[5] However, α-FAPbI$_3$ is chemically unstable; heat, light, and humidity rapidly degrade its photovoltaic performance, and this shortcoming impedes its commercialization.

The instability of α-FAPbI$_3$ is caused by its tendency to degrade and easily form the nonperovskite phase δ-FAPbI$_3$ at low temperatures, which commences dominantly at grain boundaries.[6] Use of low dimensional (LD) perovskite as passivator improves chemical stability compared to that of α-FAPbI$_3$ alone. When a small amount (<5 mol%) of LD perovskite is added into 3D α-FAPbI$_3$ perovskite, a binary mixture of 3D and LD perovskite forms as a result of thermodynamic stability.[7] LD perovskite is composed of one- or two-dimensionally connected PbI$_6$ octahedra separated by large organic spacer ions.[8,9] The organic spacer is hydrophobic; thus, compared to 3D perovskite, LD perovskite has superior resistance to hydration induced degradation.[10,11]

Several effective LD perovskites have been attempted and optimized in perovskite solar cells (PSCs), including phenylethylammonium, octylammonium, and halogenated alkylammonium lead iodide. [12,13] However, in most of the related previous studies involving the development of organic spacers, researchers have focused on hydrophobicity and π–π interactions.[13–16] The influence of the structure of LD perovskite on the crystallinity and optoelectrical property of formamidinium perovskite has rarely been discussed.[17,18] In the present study, we report that structural arrangement of PbI$_6$ octahedra in LD perovskite is one of the most critical factors for fabricating high performance LD/3D PSCs.

The crystallinity of formamidinium perovskite depends on δ-to-α phase transformation process because δ-phase is structurally favored at ambient temperature.[19–21] In the present work, from a kinetic study using Johnson–Mehl–Avrami–Kolmogorov (JMAK) model, we discover a hidden influence of the LD perovskite structure on the formation of formamidinium perovskite. First, face-sharing PbI$_6$ octahedra in LD perovskite hinders the formation of α-FAPbI$_3$, resulting in structural disorder and a high defect concentration. Second, LD perovskite with a coherent interface can nucleate epitaxial α-FAPbI$_3$ formation on LD/FAPbI$_3$ interface. We found that, among LD perovskites, phenylmethylammonium lead iodide (PMA$_2$PbI$_4$) facilitated the crystallization of α-FAPbI$_3$, improving the crystal quality by reducing microstrain in the film. The LD/3D PSC based on 1.6 mol% PMA$_2$PbI$_4$ and 98.4 mol% Cs$_{0.02}$FA$_{0.98}$PbI$_3$ had excellent carrier transport and low trap assisted recombination, resulting in the film exhibiting a PCE of 21.25% in a reverse scan. In addition, the PSC retained 80% of its initial PCE after exposure to an environment with 60% relative humidity (RH) for 20 days.

S. Song, Dr. S. J. Yang, Dr. W. Choi, Dr. H. Lee, W. Sung, C. Park,
Prof. K. Cho
Department of Chemical Engineering
Pohang University of Science and Technology
Pohang 37673, Korea
E-mail: kwcho@postech.ac.kr

The ORCID identification number(s) for the author(s) of this article can be found under https://doi.org/10.1002/aenm.202001759.

DOI: 10.1002/aenm.202001759

2. Results and Discussion

2.1. Phase Transformation Behavior of $FAPbI_3$/LD Bilayer Film

$FAPbI_3$ is more stable in the nonperovskite δ-phase at low temperatures, which makes the fabrication of a uniform and crystalline α-$FAPbI_3$ film difficult. Sublimation of compounds and residual strains that evolve under phase transformation have been associated with high defect concentrations and the nonradiative recombination of charge carriers.[20,22,23] Therefore, control of δ-to-α phase transformation is critical for fabricating efficient PSCs.

In traditional inorganic materials and crystalline solids, epitaxial transformation has been widely used to control the crystallization process of phase-pure materials. [24] For instance, α-Al_2O_3 can be grown on α-Fe_2O_3 seed crystals or CoCr alloys via solid-phase epitaxy.[25] To understand the effect of the structure of LD perovskite on phase transformation of $FAPbI_3$, different types of organic spacers were used and we conducted time-dependent X-ray diffraction (XRD) measurements (Figures S1 and S2, Supporting Information). LD perovskites were formed on δ-$FAPbI_3$ film by in situ synthesis[15] and subsequently annealed at $T = 150$ °C (**Figure 1**a). The organic spacer salts used in this experiment are bromoethylammonium (BEA) bromide, phenylmethylammonium (PMA) iodide, butylammonium (BA) iodide, phenylethylammonium (PEA) iodide, and phenylpropylammonium (PPA) iodide (Figure 1c). An LD perovskite can be classified as Class I, which is a Ruddlesden–Popper (R–P) type with corner-sharing PbI_6 octahedra, or Class II, which is a 1D or 1D–2D hybrid type with an incoherent interface with a 3D perovskite.[26] All of these organic spacer salts except PPA form an R–P-type LD perovskite.[27] Previous

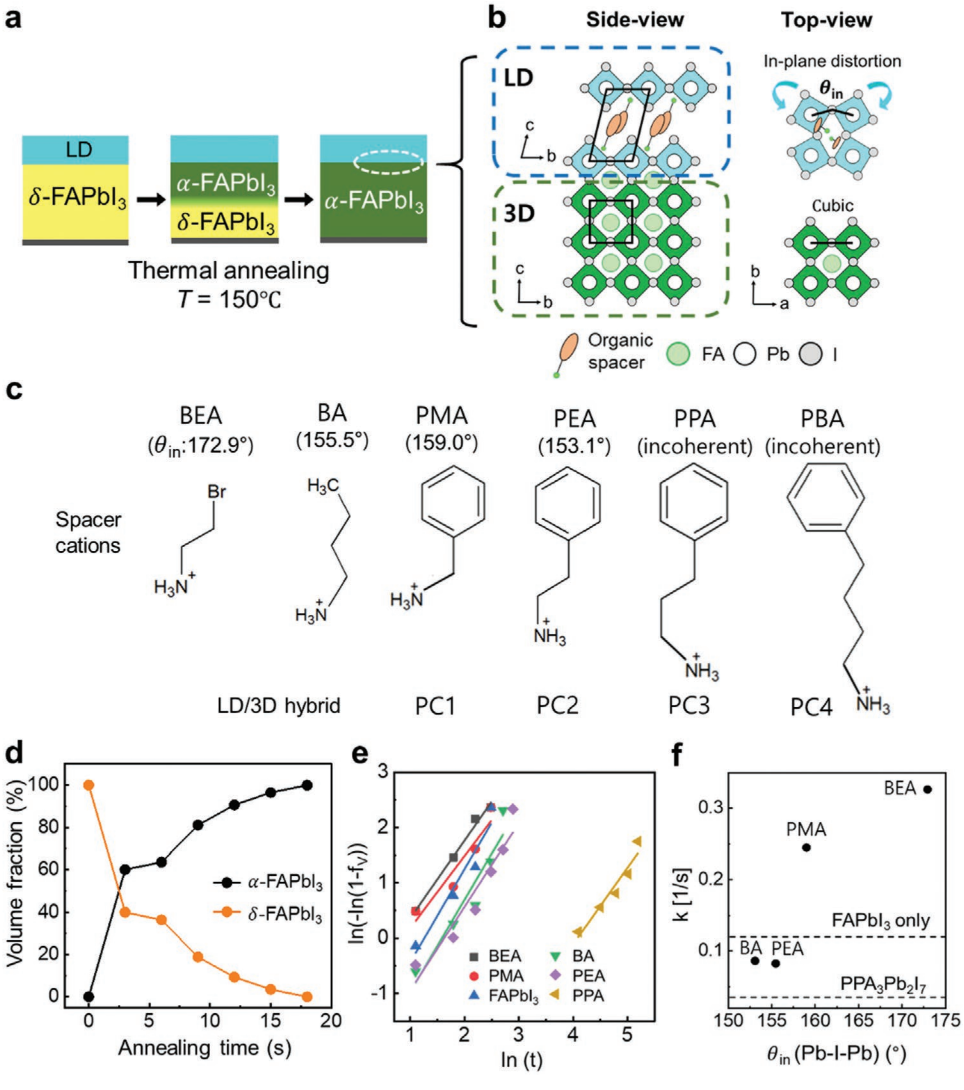

Figure 1. Kinetics of δ-to-α phase transformation of LD/δ-$FAPbI_3$ bilayer films. a) Schematics of the LD/3D hybrid perovskite film processing (detailed description in Figure S1 in the Supporting Information). b) Projected view of perovskite crystals at LD/3D perovskite interface and distortion of in-plane connection between PbI_6 octahedra. c) Molecule structure of organic spacer cations and Pb–I–Pb connection angle of the corresponding LD perovskite crystals. d) Change of volume fraction profile of α and δ phases of $FAPbI_3$ film capped with PEA_2PbI_4 for various thermal annealing times. e) Double logarithmic Avrami plot of LD/3D bilayer film. f) Rate constants obtained from JMAK equation.

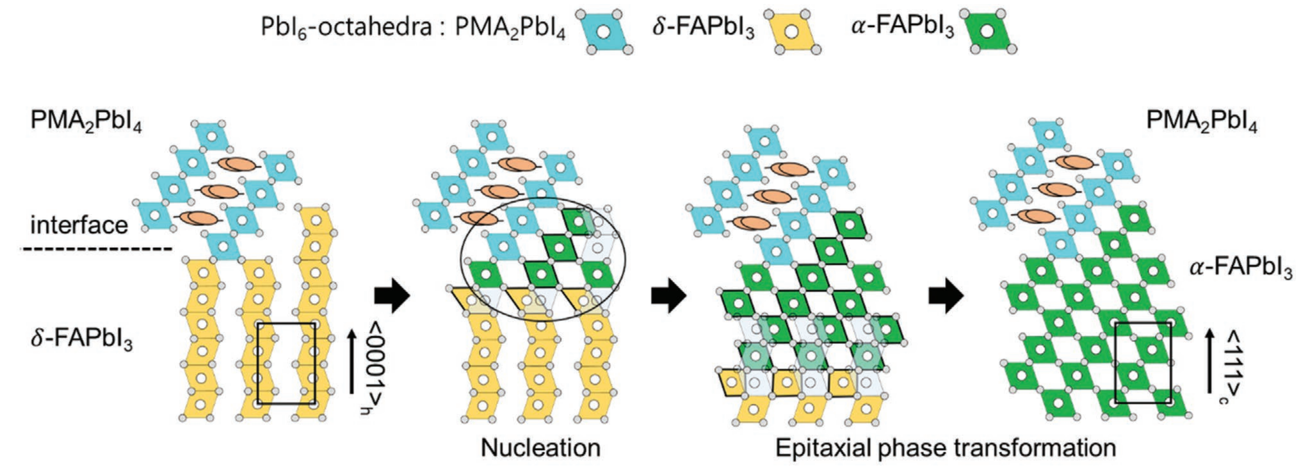

Figure 2. Schematic illustration of the epitaxial δ-to-α phase transformation of $FAPbI_3$ on the PMA_2PbI_4/δ-FAPbI3 interface (formamidinium cations are omitted).

studies have revealed that PPA disrupts the corner-sharing of PbI_6 octahedra, thereby resulting in a complex structure containing face-sharing Pb_3I_{10} trimers.[27,28]

R–P-type LD perovskites can form coherent interface with a 3D perovskite; however, the mechanical strain evolves at the interface due to the structural difference and the strain depends on the specific combination of the two materials.[18] Compared with the cubic structure of α-$FAPbI_3$, LD perovskites exhibit in-plane and out-of-plane tilting of their PbI_6 octahedra, where the out-of-plane distortion angle is usually less than 5°. Meanwhile, most LD perovskites have an in-plane Pb–I–Pb angle (θ_{in}) smaller than 155°, which differs from that of α-$FAPbI_3$ by more than 25° (Figure 1b,c).[8,18,27–29] This difference in structure tends to destabilize the $FAPbI_3$/LD interface.

The kinetics of the phase transformation is described by the JMAK model (Figure 1d–f). Volume fraction of α and δ phases of $FAPbI_3$ can be obtained from the integrated peak intensity of $(001)_\alpha$ and $(100)_\delta$ in X-ray diffraction pattern and structural parameters[30] (the detailed information is provided in Note S1 in the Supporting Information). The results of LD/3D perovskites with different organic spacers show a correlation between θ_{in} and rate constant (k) of the transformation (Figure 1f). LD perovskites based on BEA and PMA have large θ_{in} of 172.9° and 159.9°, respectively.[29] The rate constants increased from 0.12 for pure δ-$FAPbI_3$ to 0.33 and 0.24 s^{-1} for the LD/3D hybrid film made of BEA/$FAPbI_3$ and PMA/$FAPbI_3$, respectively. These results imply that the interface of the BEA/$FAPbI_3$ and PMA/$FAPbI_3$ facilitates α-$FAPbI_3$ formation. Meanwhile, LD perovskites formed with PEA and BA have lower θ_{in} angles of 153.1° and 155.5°, which differ much more from that of α-$FAPbI_3$.[18,27] The rate constants associated with α-$FAPbI_3$ formation decreased to 0.086 and 0.082 s^{-1} in the case of the PEA/$FAPbI_3$ and BA/$FAPbI_3$. This result is caused by the lattice mismatch between the LD perovskite and α-$FAPbI_3$. Mechanical strain on the interface structure makes nucleation of α-$FAPbI_3$ formation less favorable. Importantly, LD perovskites with face-sharing PbI_6 octahedra strongly suppress the formation of α-$FAPbI_3$. The rate constant for $FAPbI_3$/PPA is 0.0036 s^{-1}, which is lower than that for the δ-$FAPbI_3$-only film. δ-$FAPbI_3$ has a 1D structure composed of face-sharing PbI_6 octahedra. It can be inferred that LD perovskites apparently stabilize δ-$FAPbI_3$ and further increase the E_a required for the formation of α-$FAPbI_3$.

To understand the mechanism of phase transformation process, crystal-structural evolution of PMA/$FAPbI_3$ during thermal annealing was investigated by grazing-incidence wide-angle X-ray scattering (GIWAXS). X-ray incident angle was fixed at either 0.12° or 0.5° to probe the near surface and bulk of the perovskite film, respectively (Figures S3 and S4, Supporting Information). To quantify the volume fraction of α-$FAPbI_3$, we compared the diffraction peak area of $(001)_\alpha$ and $(100)_\delta$ in the azimuthally integrated intensity plot (Figure S5, Supporting Information). The surface of PMA/$FAPbI_3$ film without thermal annealing exhibits 58% of α-$FAPbI_3$, which suggests that spin-coating of PMA-I on the δ-$FAPbI_3$ does not only form PMA_2PbI_4 capping layer, but also induces the nucleation of α-$FAPbI_3$ formation. On the other hand, there is a larger amount of δ-$FAPbI_3$ in the bulk than near the surface. The difference between surface and bulk composition reflects the nucleation of phase transformation occurs dominantly at the interface of PMA_2PbI_4/$FAPbI_3$ and then, phase transformation propagates toward the bulk.

The aforementioned results suggest a scheme of epitaxial phase transformation (**Figure 2**). Phase transformation of $FAPbI_3$ is known to occur via translation of atoms.[31] If the PbI_6 framework of PMA_2PbI_4 contacts δ-$FAPbI_3$, it can function as a template for the growth of α-$FAPbI_3$. The rearrangement of atoms begins at the interface, disconnecting face-sharing PbI_6 octahedra; the rearrangement then propagates toward bulk regions until the structure is completely transformed into α-$FAPbI_3$ (Figure S6, Supporting Information).

2.2. Structural Evolution of Hybrid Perovskite

LD/3D hybrid perovskite films were prepared with a combination of 98.4 mol% of $Cs_{0.02}FA_{0.98}PbI_3$ (3D) and 1.6 mol% of LD perovskite; this concentration of LD perovskite was chosen because it yields a LD/3D PSC with the highest PCE and greatest reproducibility (Figures S7 and S8, Supporting Information). PSCs with excess LD perovskite exhibited increased hysteresis and lower V_{oc} (Table S1, Supporting Information). LD perovskites

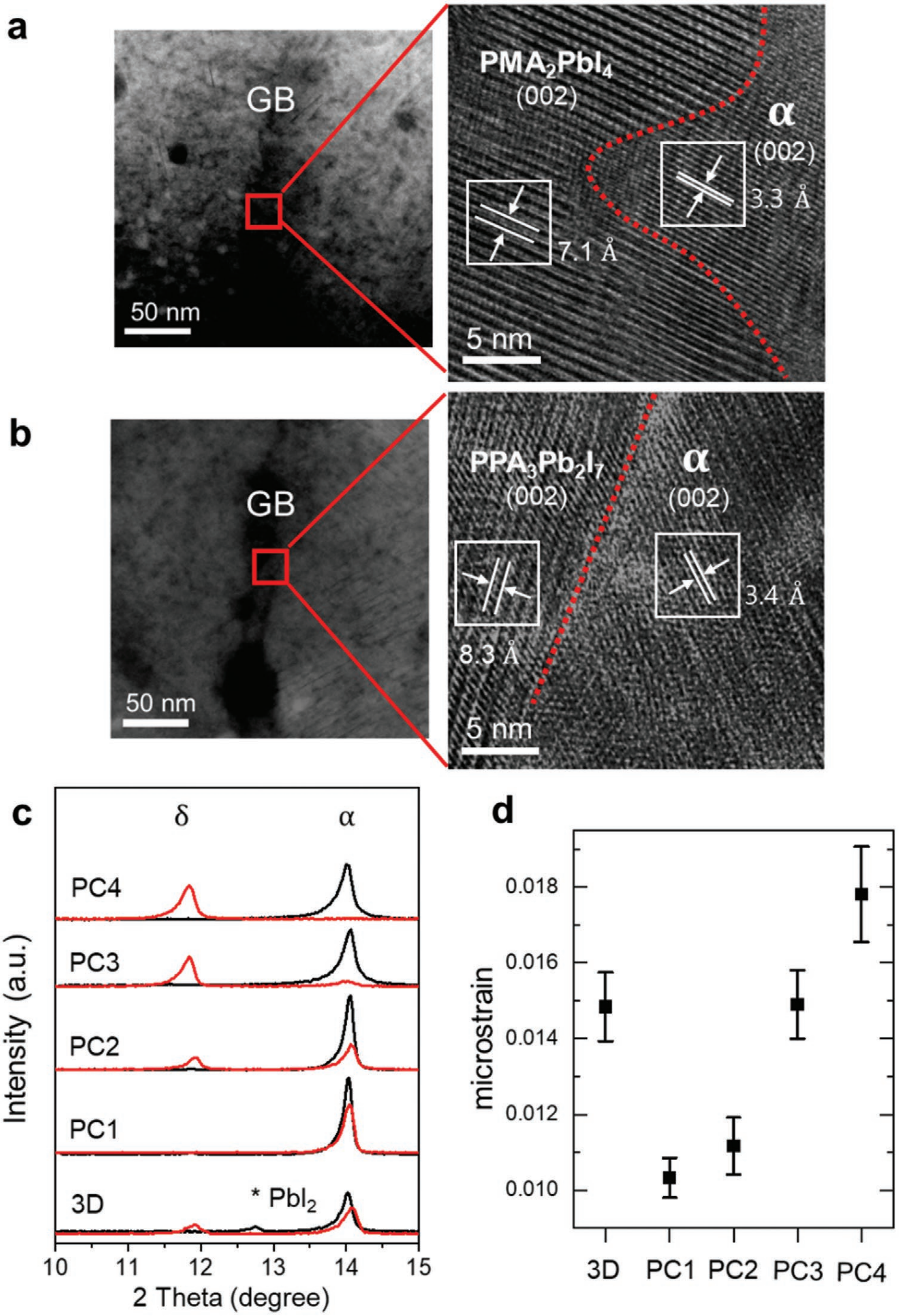

Figure 3. TEM image of LD/α-FAPbI$_3$ including grain boundaries (GB): a) PC1; b) PC3. STEM images (right) were obtained from the highlighted area. c) XRD patterns of preannealed (red) and annealed (black) perovskite films. d) Microstrain obtained from modified Williamson–Hall plot.

were made from PMA, PEA, PPA, and phenylbutylammonium (PBA) iodide. The structural arrangement of LD perovskites is governed by the molecular structure of their organic spacer cations. PMA and PEA form an R–P structure (structural formula A_2PbI_4), whereas PPA and PBA form a 1D–2D hybrid structure (structural formula $A_3Pb_2I_7$), which includes face- and corner-sharing PbI_6 octahedra.[27] We hereafter refer to the reference 3D perovskite film simply as “3D” and to the LD/3D hybrid films by the length of the carbon-atom chain connected to the phenyl group used for the organic spacer, i.e., “PC1,” “PC2,” “PC3,” and “PC4,” corresponding to PMA, PEA, PPA, and PBA, respectively.

The structures of the PC1 and PC3 hybrid perovskite films were investigated by transmission electron microscopy (TEM) (**Figure 3**a,b). The grain-boundary region was magnified, revealing two regions that clearly differ. The interplanar distance of crystals in these two regions was calculated by fast Fourier transform (FFT) (Figure S9, Supporting Information). The FFTs of the grain-boundary regions show interplanar distances of 7.1 and 8.3 Å, which well match the (002) reflection in the XRD patterns of PMA_2PbI_4 and $PPA_3Pb_2I_7$, respectively (Figure S10, Supporting Information). Meanwhile, the interior region shows an interplanar spacing of 3.3 Å, which corresponds to the (002) reflection of α-$Cs_{0.02}FA_{0.98}PbI_3$. We confirmed that the LD/3D perovskite film was composed of a 3D perovskite with its grain boundary filled with an LD perovskite.

Analysis of the optical absorbance spectra indicated that the 3D and LD/3D perovskites exhibit an almost identical bandgap of 1.53 eV (Figure S11, Supporting Information). Meanwhile, the absorption spectra of preannealed samples show different results. The spectra of 3D, PC1, and PC2 show an absorption onset near 820 nm, which is characteristic of the α-phase, whereas the spectra of PC3 and PC4 show a blue-shifted absorption onset (Figure S12, Supporting Information). The spectra of PC3 and PC4 also show suppressed phase transformation at T = 150 °C. The preannealed film remained yellow for an extended period (Figure S13, Supporting Information); this color is characteristic of the δ-phase.

Similar results are shown in the XRD patterns of preannealed perovskite films. The materials in preannealed film had assembled into either the α-phase or the δ-phase (Figure 3c). Compared with the 3D and PC2 films, the PC1 film promoted the formation of pure α-phase. The XRD pattern of PC1 shows only a sharp (001) peak near 14° arising from its cubic structure, whereas the patterns of the other films show mixtures of the α and δ phases. By contrast, PC3 and PC4 promoted δ-phase formation (their XRD patterns show a peak near 11.8°) and suppressed formation of the α-phase.

Surface views of the final perovskite films show similar morphologies, with grain sizes of 100–500 nm (Figure S14, Supporting Information). However, the films show different time evolutions of their morphologies. We characterized the morphology of films subjected to different thermal annealing times at T = 150 °C. The 3D and PC1 films formed large α-phase grains within 2 min (Figure S15, Supporting Information). However, the PC3 and PC4 films have small δ-phase grains that slowly transformed and assembled into α-phase grains (Figure S16, Supporting Information). Consequently, we verified that LD perovskites surrounding the grain boundary of a 3D perovskite have a dominant effect on nucleation of the phase transformation.

The presence of crystal imperfections and structural defects, including dislocations, vacancies, and microdomains, causes variations in the lattice spacing. We quantified structural disorder by using a modified Williamson–Hall method.[22] In the XRD patterns of crystalline materials with a grain size larger than 100 nm, peak broadening is attributed to microstrain in the crystal. Microstrain can be obtained from the slope of a plot of $(\Delta d_{\mathrm{obs}}^2 - \Delta d_{\mathrm{ins}}^2)^{1/2}$ versus d_{hkl} obtained from the diffraction peaks of α-phase perovskite (Figure S18, Supporting Information). Δd_{obs} is full width half maximum (fwhm) measured for each (hkl) plane and d_{ins} is fwhm from the instrument, which can be obtained from LaB_6 standard. As the alkyl chain length of phenylalkylammonium increased, the microstrain increased monotonically: 0.0156 for 3D; 0.0126 for PC1; 0.0137 for PC2; 0.0169 for PC3; 0.0180 for PC4 (Figure 3d). Crystal deformation under phase transformation makes an anisotropic strain tensor, which can be relieved through formation of point defects and twin boundaries.[20] These microstresses can be minimized by lowering the temperature required for the formation of α-$FAPbI_3$.[21] PC3 and PC4 form pure δ-phase in preannealed state and require the perovskite material to proceed δ-to-α phase transformation during film formation (Figure 3c). Therefore, PC3 and PC4 have higher microstrain than that of 3D film. Meanwhile, PC1 already forms pure α-phase in preannealed film, so there are no extra strains evolved during thermal annealing process.

2.3. Photoluminescence (PL) Properties of LD/3D Hybrid Perovskite

The PL properties of the perovskite films were investigated using PL measurements. We qualitatively compared the charge-trap density among perovskite films on the basis of their steady-state PL intensity (**Figure** 4a). Deep traps (i.e., Shockley–Read–Hall (SRH) recombination centers) are located near the middle of the bandgap. Charges trapped in the deep traps in PSCs would recombine nonradiatively, reducing charge extraction.[2,3,32] The integrated PL intensity of PC1, PC2, PC3, and PC4 was 142.8%, 122.0%, 116.7%, and 65.6% of the PL intensity of the 3D film, respectively. The increased PL intensity in PC1 and PC2 was attributed to the extended PL lifetime (Figure 4b).

Transient PL decays were fitted using a double-exponential decay curve (Table S2, Supporting Information)

$$y = y_0 + A_1 \cdot \exp(-t/\tau_1) + A_2 \cdot \exp(-t/\tau_2) \tag{1}$$

The fitted time constants consist of a fast component τ_1 (τ_1 < 10 ns) and a slow component τ_2 ($\tau_1 \approx$ 100 ns). The fast-decay component was assigned to charge-carrier trapping induced by trap states that formed as a result of structural disorder such as vacancies or interstitial defects; the slow-decay component was assigned to radiative recombination of free carriers.[33] With the addition of LD perovskite, PMA_2PbI_4, PEA_2PbI_4, $PPA_3Pb_2I_7$, or $PBA_3Pb_2I_7$, the fast-decay component τ_1 changed from 7.0 to 15.7, 14.8, 13.7, and 7.1 ns, respectively, and the slow-decay parameter τ_2 changed from 50.4 to 154.1, 126.3, 87.8, or 52.9 ns, respectively. As a result, the average PL lifetime changed from 28.3 to 101.3 to 75.9 to 46.7 to 27.2 ns. Although all of the LD perovskites passivated the grain boundary of the 3D perovskite, the crystallinity of the 3D perovskite grain is different among the LD/3D hybrids. In the case of PC1, the crystallinity of the perovskite film could be further improved by inducing the nucleation of α-$FAPbI_3$ by mixing with an LD perovskite. However, $PPA_3Pb_2I_7$ and $PBA_3Pb_2I_7$ hinder the formation of α-$FAPbI_3$ and induce lattice strain during the thermal annealing process. As a result, uncontrolled phase transformation of $FAPbI_3$ resulted in a high density of defects, which causes nonradiative recombination losses.[14,20,34]

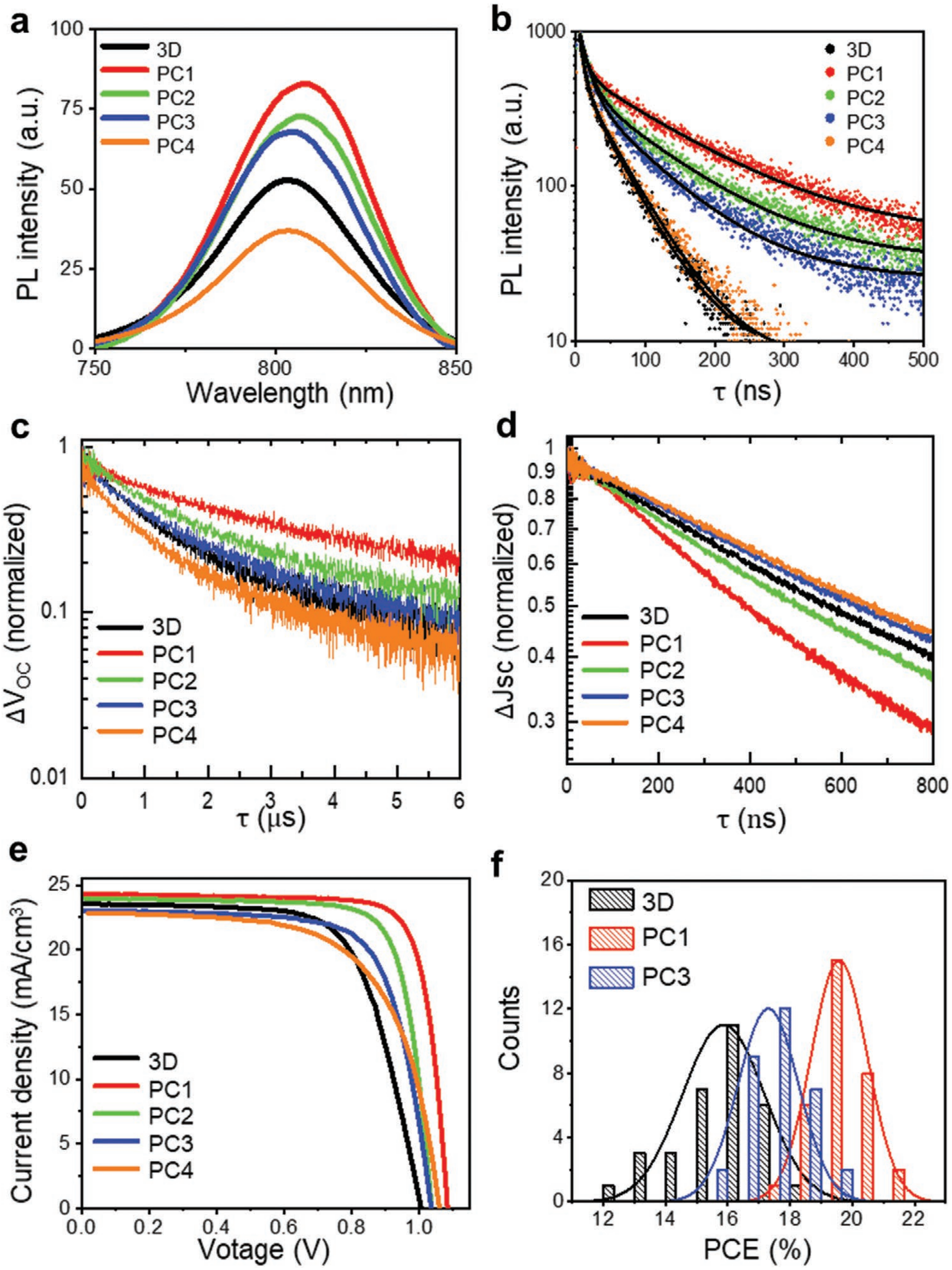

Figure 4. Charge-carrier dynamics and photovoltaic performance. a) Steady-state and b) time-resolved PL spectra of the perovskite films. c) Transient photovoltage and d) transient photocurrent of PSCs. e) Current density–voltage (*J*–*V*) curves of PSCs. f) Power conversion efficiency (PCE) distribution of the perovskite devices.

2.4. Charge-Carrier Transport Properties of LD/3D Hybrid Perovskite

We further compared the charge-carrier transport properties on the basis of electrical measurements. To study charge-carrier dynamics during device operation, we measured the transient photovoltage (TPV) and transient photocurrent (TPC). During operation of a PSC device, photogenerated charge carriers are collected at selective contacts or recombine through the trap states. The decay of TPV traces the decay of excess carriers under the open-circuit condition (Figure 4c).[13,35] Carriers mainly recombine by SRH recombination; therefore, the lifetime extracted from a single-exponential decay $\Delta V_{\mathrm{oc}} = \Delta V_{\mathrm{oc,\,0}} \exp(-t/\tau_{\mathrm{TPV}})$ can be used to determine the carrier lifetime (τ_{TPV}). The carrier lifetime increased from 1.11 to 2.36, 1.43, or 1.37 μs with the addition of $\mathrm{PMA_2PBI_4}$, $\mathrm{PEA_2PbI_4}$, or $\mathrm{PPA_3Pb_2I_7}$, respectively, but decreased to 1.02 μs with addition of $\mathrm{PBA_4Pb_2I_7}$.

The decay of TPC was measured under the short-circuit condition, where an external circuit was connected to a small resistor with a resistance *R* of 50 Ω (Figure 4d).[13,35] Charge carriers were swept out of the device and quickly recombined through an external circuit. Thus, the TPC curve illustrates the carrier transit time across the bulk perovskite and the electrode interface. The transit times were extracted from a single-exponential decay $\Delta J_{sc} = \Delta J_{sc0}\exp(-t/\tau_{TPC})$, where τ_{TPC} changed from 0.711 to 0.451, 0.59, 0.821, or 0.973 µs with the addition of PMA_2PbI_4, PEA_2PbI_4, $PPA_3Pb_2I_7$, or $PBA_3Pb_2I_7$, respectively. τ_{TPC} becomes shorter with PMA_2PbI_4 and PEA_2PbI_4. However, τ_{TPC} longer with $PPA_3Pb_2I_7$ and $PBA_3Pb_2I_7$. The elongated transit time for $PPA_3Pb_2I_7$ and $PBA_3Pb_2I_7$ originates from decreased effective charge-carrier mobility by increased trap density.

The densities of charge-carrier defects in perovskite films have been confirmed using space-charge-limited-current (SCLC) analysis.[35,36] Electron-only devices were fabricated (Figure S19, Supporting Information). The electron trap density n_t was obtained from the relationship $V_{TFL} = \exp(n_t L^2/(2\varepsilon\varepsilon_0))$, where V_{TFL} is voltage at which trap filling begins, L (=500 nm) is the thickness of the perovskite layer, and ε (=32) is the relative dielectric constant of the perovskite. The estimated trap densities were 1.04×10^{16} cm^{-3} for 3D, 7.03×10^{15} cm^{-3} for PC1, 8.23×10^{15} cm^{-3} for PC2, 8.68×10^{15} cm^{-3} for PC3, and 1.05×10^{16} cm^{-3} for PC4. In summary, PC1 and PC2 exhibited superior performance in that they showed a low trap density, prolonged free-carrier lifetime, and efficient carrier extraction, PC4 exhibited a high trap density, which resulted in a short carrier lifetime, and PC3 exhibited a small enhancement in photoelectric properties compared with those of 3D.

2.5. Highly Efficient and Stable LD/3D Perovskite Using PMA_2PbI_4 Additive

The current density–voltage (J–V) characteristics were obtained from typical photovoltaic devices based on 3D or LD/3D perovskites. To quantify the degree of hysteresis, we define a hysteresis index HI = $(PCE_{reverse} - PCE_{forward}))/PCE_{reverse}$, where $PCE_{reverse}$ is the PCE from the reverse voltage sweep and $PCE_{forward}$ is the PCE from forward voltage sweep (**Table 1**). The addition of a small amount of an LD perovskite induced concurrent increases in the V_{oc}, J_{sc}, and the fill factor (FF). Hence, PC1 achieved a maximum efficiency of 21.25% (Figure 4e). The remarkable increase in the V_{oc} and FF might be a result of reduced nonradiative charge-carrier recombination due to increased crystal perfection as already shown in Figure 3. Interfacial charge accumulation by charge carrier trapping is the main contributor to hysteresis behavior [3] The trend of the HI is consistent with the trend of the trap density (n_t) extracted from SCLC measurements (Figure S19, Supporting Information). Hysteresis was weak in PC1 and PC2 but strong in PC3 and PC4. Integration over the wavelength of the external quantum efficiency (EQE) (Figure S22, Supporting Information) reveals that the integrated currents in 3D, PC1, PC2, PC3, and PC4 were 21.77, 23.60, 22.68, 21.84, and 20.44 mA cm^{-2}, respectively, which are 92.6%, 95.9%, 94.5%, 92.9%, and 89.6% of the J_{sc} measured under a reverse J–V scan, respectively (Figure 4e). The EQE increase in the long wavelength (600–800 nm) in PC1 and PC2 is attributed to the reduction of bulk defect induced recombination, enabling charge carriers excited by long wavelength photons to travel though the perovskite film for extraction.[37] The EQE increase in short wavelength (300–400 nm) might be originated from the efficient charge extraction at the electron transport layer (ETL)/perovskite interface. A stabilized efficiency of 19.95% was obtained with PC1; this efficiency is very similar to the PCE obtained in a reverse scan (Figure S23, Supporting Information). The PCE histogram (Figure 4f) shows that average PCE of PC1 was 19.58% and was highly reproducible, with a standard deviation of 0.90% (n = 32 independent devices). The PCE deteriorates monotonically with increasing alkyl chain length of phenylalkylammonium ion, and the average PCE of PC4 (14.86 ± 1.16%) was similar to that of 3D.

Table 1. Typical photovoltaic parameters of 3D and LD/3D PSCs.

	Scanning mode	V_{oc} [V]	J_{sc} [mA cm^{-2}]	FF	PCE [%]	Hysteresis index [%]
3D	Reverse	1.01	23.5	0.68	16.08	43.97
	Forward	0.91	22.7	0.43	9.01	
PC1	Reverse	1.08	24.3	0.81	21.25	3.24
	Forward	1.08	24.3	0.76	20.01	
PC2	Reverse	1.04	24.0	0.78	19.34	3.13
	Forward	1.04	24.1	0.71	17.95	
PC3	Reverse	1.04	23.5	0.71	17.45	7.97
	Forward	1.01	23.5	0.69	16.06	
PC4	Reverse	1.06	22.8	0.65	15.58	17.46
	Forward	1.04	22.7	0.54	12.86	

The environmental instability of perovskite-based devices remains a challenging problem. We performed two stability tests under a controlled environment without any encapsulation (**Figure 5**a,b). First, the device was stressed using continuous

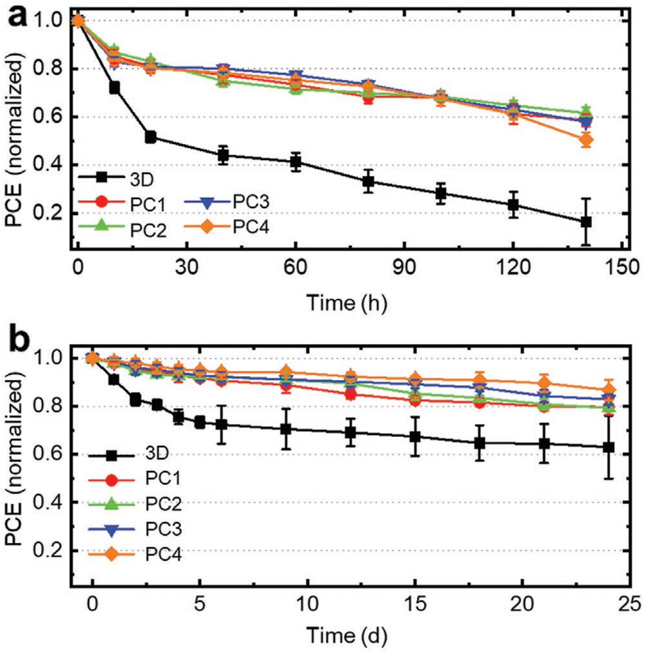

Figure 5. Improved stability of the LD/3D hybrid perovskite solar cells by the addition of LD perovskites. a) PCE decays of the corresponding solar cells under the continuous illumination 100 mW cm^{-2} with RH 35% under open-circuit condition without any encapsulation. b) PCE decays of devices stored under the dark condition with controlled RH 60% without any encapsulation. PCE was measured from six different devices for each stability test.

illumination at 1 sun (100 mW cm^{-2}) under the open-circuit condition and at an RH of 35%. After 80 h, the normalized efficiency decreased to ≈30% of the initial value in the case of a pristine 3D PSC but remained at 70% of the initial value in the case of LD/3D PSCs. The second stability test was done for 25 days in darkness with RH controlled at 60% by using unencapsulated devices. The normalized efficiency decreased to 75% in the pristine device after 5 days, but remained >90% in the LD/3D hybrid device. These results are consistent with previous reports that LD perovskites with large organic spacers are hydrophobic and resistant to degradation by moisture.[10,13]

To quantify how LD/3D hybridization affects the hydrophobicity of the surface of a perovskite, we measured the corresponding water contact angles θ (Figure S24, Supporting Information). The θ of the pristine 3D film was 66.7°, whereas those of films of PC1, PC2, PC3, and PC4 were 72.1°, 72.2°, 76.9°, and 81.9°, respectively. This increase in θ indicates that the surface of the LD/3D perovskite films is more hydrophobic than that of the 3D film and can therefore repel moisture and slow water infiltration into the perovskite film in a moist environment. The hydrophobicity of LD perovskite crystals incorporated to the grain boundary in the LD/3D hybrid perovskite suppresses the accumulation of water molecules on the $Cs_{0.02}FA_{0.98}PbI_3$; otherwise, the grain boundary is easily hydrated.

Unencapsulated perovskite films were aged at 60% RH in the darkness for 10 days, and their XRD patterns were subsequently recorded (Figure S25, Supporting Information). The pristine sample had degraded to PbI_2 and δ-phase perovskite; however, the LD/3D hybrids maintained their phase purity. The modified surface of the LD/3D perovskites repelled moisture, preventing its accumulation on grain boundaries; thus, hydration, which would have caused unwanted phase transition, did not occur.

3. Conclusions

Our study reveals that the crystallinity and electronic properties of FA perovskite can be substantially enhanced by mixing with an LD perovskite with a similar arrangement of PbI_6 octahedra. We proposed that the structure of the LD perovskite affects the kinetics of formamidinium perovskite formation during thermal annealing. When a small amount of PMA_2PbI_4 was present, we observed reduced microstrain in the perovskite film, which implies a reduction in its structural disorder. As a result of the high film quality, the LD/3D perovskite film exhibited enhanced PL properties and excellent charge transport. Finally, a PSC with the highest PCE = 21.06% in the reverse current–voltage scan and stabilized PCE of 19.95%. We speculate that this report will guide the development of other LD/3D hybrid perovskite materials that have a photoinactive δ-phase, such as $CsPbI_3$ and $FASnI_3$.

4. Experimental Section

Materials: All chemicals and reagents were used as received without any further purification. Fluorine-doped tin oxide (FTO) was purchased from Pilkington (TEC8). Lead iodide (PbI_2) 99.99% was purchased from TCI. Cesium iodide (CsI) 99.998% was purchased from Alfa Aesar. $HC(NH_2)_2I$ (FAI) was purchased from Dyesol. Phenyl-C61-butyric acid methyl ester (PCBM) 99.5% was purchased from Soleene BV. Spiro-MeOTAD was purchased from Lumtec. Tin chloride ($SnCl_2$) (99.99%), *N*-methyl-2-pyrrolidone (NMP) anhydrous (99.8%), *N*,*N*-dimethylformamide (DMF) anhydrous (99.8%), chlorobenzene (CB) anhydrous (99.8%), and bis(trifluoromethane)sulfonimide lithium salt (LiTFSI) (96%) were purchased from Sigma-Aldrich.

Synthesis of Phenylalkylammonium Iodide: First, 2.7 mL of hydroiodic acid (57 wt% in water) was dropped slowly into a solution of 3.6 g phenylalkylamine in ethanol placed in ice bath. The solution was stirred for 5 h, and then the solvent was removed using a rotary evaporator. The resulting solid was washed with diethyl ether several times until the color changed to white. The crystals were filtrated and dried in vacuum at 55 °C.

Device Fabrication: PSCs were fabricated in a planar heterojunction-type structure, FTO/compact-SnO_2/perovskite/spiro-OMeTAD/Au. FTO glass was cleaned with detergent, deionized (DI) water, acetone, and 2-propanol in sequence, each with ultrasonication for 20 min. The cleaned substrates were further treated with UV-ozone to increase the wettability. A 0.03 м $SnCl_2$ solution in ethanol was spin coated on the substrate at 3000 rpm for 30 s, and then heat treated at 150 °C for 30 min. The coated substrate was cooled to room temperature, then $SnCl_2$ solution was spin coated once again, and then thermally annealed at 150 °C for 1 min and then at 180 °C for 40 min. The FTO/SnO_2 substrate was treated with UV-ozone to make a hydrophilic surface before deposition of perovskite. Perovskite precursor material was prepared with stoichiometric ratio of CsI, FAI, and PbI_2. For 2D/3D hybrid perovskite, 1.6 mol% of 2D perovskite and 98.4 mol% 3D perovskite precursor were mixed together. Precursor was dissolved in mixed solvent of DMF and NMP (5:1 vol/vol). The 1.66 м perovskite solution was spin coated at 4400 rpm for 20 s; and 10 s into this spin cycle, 0.8 mL of diethyl ether was dripped onto the surface. Thermal annealing was immediately performed at 100 °C for 1 min to drive off the NMP. Then, the preannealed film was transferred to 150 °C to obtain cubic formamidinium perovskite. The hole transport layer (HTL) solution consisting of 85.8 mg of spiro-MeOTAD in 1 mL of chlorobenzene was doped with 33.8 µL of 4-*tert*-butylpyridine and 19.3 µL of Li-TFSI (520 mg mL^{-1} in acetonitrile) solution. The 20 µL of the HTL solution was loaded onto the perovskite substrate and spin coated at 2000 rpm for 30 s. All of the preparation and deposition process was performed in ambient condition (T < 25 °C, RH < 45%). The Au electrode (80 nm) was deposited by thermal evaporation. Electron only devices were fabricated as follows. The ETL consisting of 20 mg of PCBM in 1 mL chlorobenzene was spin coated on the FTO/SnO_2/perovskite substrate at 2000 rpm. Next, LiF (1 nm) and Ag (80 nm) were deposited by thermal evaporation.

Material Characterizations: The UV–vis absorption/transmission and PL spectra of the spin coated films were recorded using a spectrometer (Perkin Elmer, Lambda 1050) and a spectrofluorimeter (Horiba Jobin Yvon NanoLog), respectively. The surface wettabilities of the perovskite films were measured by using a contact angle meter (Krüss BSA 10) to quantify the contact angle between the DI water and the films. X-ray diffraction was performed with an X-ray diffractometer (D/MAX-2500, RIGAKU) with Cu-Kα X-rays. GIWAXS measurements were performed using the synchrotron source at the 9A beamlines at the Pohang Accelerator Laboratory (PAL) in Korea. Field emission-scanning electron microscope (FE-SEM) images were captured by Hitachi S-4800 FE-SEM system. TEM and FFTs were measured using a JOEL JEM-2200FS (with image Cs-corrector) at the National Institute for Nanomaterials Technology (NINT) in Pohang. The time-resolved photoluminescence spectroscopy (TRPL) traces were recorded by using time-correlated single photon counting (TCSPC) system (Hamamatsu/C11367-31). The conditions of the pulsed laser source for the TCSPC measurements were a wavelength of 464 nm, a repetition rate of 100 kHz, fluence of 4 nJ cm^{-2}, and a pulse width of 70 ps. All samples were excited from the bottom perovskite side with an excitation wavelength of 464 nm, and an emission wavelength of 800 nm was recorded under ambient conditions.

Solar Cell Characterizations: Current density–voltage (*J*–*V*) curves were recorded using a solar simulator (Newport, Oriel Class A) and a source meter (Keithley 4200) in a N_2-filled glove box at RT. The illumination was set to AM 1.5G and calibrated to 100 mW cm^{-2} by using Reference Cell PVM 132 calibrated at the US National Renewable Energy Laboratory. A mask was used for the *J*–*V* measurements and its area was 0.0555 cm^2. The step voltage was 10 mV and the delay time was 50 ms.

The EQE was measured using a photomodulation spectroscopy setup (Merlin, Oriel) with monochromatic light from a Xenon lamp. TPV and TPC were performed with a TDC3054C digital oscilloscope connected to high-speed reamplifiers: SR560 and DHPCA-100. The samples were excited with a 3 ns pulsed laser at 532 nm (OBB, NL4300, and OD401) under AM 1.5G illumination at an intensity of 1 sun.

Supporting Information

Supporting Information is available from the Wiley Online Library or from the author.

Acknowledgements

This work was supported by a grant (Code No. 2011-0031628) from the Center for Advanced Soft Electronics under the Global Frontier Research Program of the Ministry of Science and ICT, Korea. The authors thank the Pohang Accelerator Laboratory for providing the synchrotron radiation sources at 9A beamline used in this study.

Conflict of Interest

The authors declare no conflict of interest.

Keywords

coherent interfaces, Johnson–Mehl–Avrami–Kolmogorov analysis, low dimensional perovskites, moisture stability

Received: May 27, 2020
Revised: August 20, 2020

---

[1] Q. F. Han, S. H. Bae, P. Y. Sun, Y. T. Hsieh, Y. Yang, Y. S. Rim, H. X. Zhao, Q. Chen, W. Z. Shi, G. Li, Y. Yang, *Adv. Mater.* **2016**, *28*, 2253.

[2] M. Saliba, T. Matsui, K. Domanski, J. Y. Seo, A. Ummadisingu, S. M. Zakeeruddin, J. P. Correa-Baena, W. R. Tress, A. Abate, A. Hagfeldt, M. Gratzel, *Science* **2016**, *354*, 206.

[3] M. Abdi-Jalebi, Z. Andaji-Garmaroudi, S. Cacovich, C. Stavrakas, B. Philippe, J. M. Richter, M. Alsari, E. P. Booker, E. M. Hutter, A. J. Pearson, S. Lilliu, T. J. Savenije, H. Rensmo, G. Divitini, C. Ducati, R. H. Friend, S. D. Stranks, *Nature* **2018**, *555*, 497.

[4] a) C. Park, S. J. Yang, J. Choi, S. Song, W. Choi, K. Cho, *ChemSusChem* **2020**, *13*, 3261; b) D. H. Sin, S. B. Jo, S. G. Lee, H. Ko, M. Kim, H. Lee, K. Cho, *ACS Appl. Mater. Interfaces* **2017**, *9*, 18103; c) S. J. Yang, M. Kim, H. Ko, D. H. Sin, J. H. Sung, J. Mun, J. Rho, M.-H. Jo, K. Cho, *Adv. Funct. Mater.* **2018**, *28*, 1804067; d) R. Singh, A. Giri, M. Pal, K. Thiyagarajan, J. Kwak, J. J. Lee, U. Jeong, K. Cho, *J. Mater. Chem. A* **2019**, *7*, 7151.

[5] NREL, Best research-cell efficiencies, https://www.nrel.gov/pv/cell-efficiency.html (accessed: August 2020).

[6] a) Q. Wang, B. Chen, Y. Liu, Y. H. Deng, Y. Bai, Q. F. Dong, J. S. Huang, *Energy Environ. Sci.* **2017**, *10*, 516; b) C. Park, H. Ko, D. H. Sin, K. C. Song, K. Cho, *Adv. Funct. Mater.* **2017**, *27*, 1703546; c) Z. Wu, M. Jiang, Z. Liu, A. Jamshaid, L. K. Ono, Y. Qi, *Adv. Energy Mater.* **2020**, *10*, 1903696.

[7] C. M. M. Soe, G. P. Nagabhushana, R. Shivaramaiah, H. H. Tsai, W. Y. Nie, J. C. Blancon, F. Melkonyan, D. H. Cao, B. Traore, L. Pedesseau, M. Kepenekian, C. Katan, J. Even, T. J. Marks, A. Navrotsky, A. D. Mohite, C. C. Stoumpos, M. G. Kanatzidis, *Proc. Natl. Acad. Sci. USA* **2019**, *116*, 58.

[8] Y. N. Chen, Y. Sun, J. J. Peng, J. H. Tang, K. B. Zheng, Z. Q. Liang, *Adv. Mater.* **2018**, *30*, 1703487.

[9] M. D. Smith, E. J. Crace, A. Jaffe, H. I. Karunadasa, *Annu. Rev. Mater. Res.* **2018**, *48*, 111.

[10] a) Y. Lin, Y. Bai, Y. J. Fang, Z. L. Chen, S. Yang, X. P. Zheng, S. Tang, Y. Liu, J. J. Zhao, J. S. Huang, *J. Phys. Chem. Lett.* **2018**, *9*, 654; b) Z. P. Wang, Q. Q. Lin, F. P. Chmiel, N. Sakai, L. M. Herz, H. J. Snaith, *Nat. Energy* **2017**, *2*, 17135.

[11] a) M. H. Li, H. H. Yeh, Y. H. Chiang, U. S. Jeng, C. J. Su, H. W. Shiu, Y. J. Hsu, N. Kosugi, T. Ohigashi, Y. A. Chen, P. S. Shen, P. Chen, T. F. Guo, *Adv. Mater.* **2018**, *30*, 1801401; b) D. Bi, P. Gao, R. Scopelliti, E. Oveisi, J. Luo, M. Grätzel, A. Hagfeldt, M. K. Nazeeruddin, *Adv. Mater.* **2016**, *28*, 2910; c) P. Chen, Y. Bai, S. Wang, M. Lyu, J.-H. Yun, L. Wang, *Adv. Funct. Mater.* **2018**, *28*, 1706923; d) Y. Liu, S. Akin, L. Pan, R. Uchida, N. Arora, J. V. Milić, A. Hinderhofer, F. Schreiber, A. R. Uhl, S. M. Zakeeruddin, A. Hagfeldt, M. I. Dar, M. Grätzel, *Sci. Adv.* **2019**, *5*, eaaw2543.

[12] a) G. Liu, H. Zheng, X. Xu, S. Xu, X. Zhang, X. Pan, S. Dai, *Adv. Funct. Mater.* **2019**, *29*, 1807565; b) G. Grancini, C. Roldan-Carmona, I. Zimmermann, E. Mosconi, X. Lee, D. Martineau, S. Narbey, F. Oswald, F. De Angelis, M. Graetzel, M. K. Nazeeruddin, *Nat. Commun.* **2017**, *8*, 15684; c) Y. Y. Cho, A. M. Soufiani, J. S. Yun, J. C. Kim, D. S. Lee, J. Seidel, X. F. Deng, M. A. Green, S. J. Huang, A. W. Y. Ho-Baillie, *Adv. Energy Mater.* **2018**, *8*, 1703392.

[13] J. W. Lee, Z. H. Dai, T. H. Han, C. Choi, S. Y. Chang, S. J. Lee, N. De Marco, H. X. Zhao, P. Y. Sun, Y. Huang, Y. Yang, *Nat. Commun.* **2018**, *9*, 3021.

[14] M. Jung, T. J. Shin, J. Seo, G. Kim, S. I. Seok, *Energy Environ. Sci.* **2018**, *11*, 2188.

[15] K. T. Cho, G. Grancini, Y. Lee, E. Oveisi, J. Ryu, O. Almora, M. Tschumi, P. A. Schouwink, G. Seo, S. Heo, J. Park, J. Jang, S. Paek, G. Garcia-Belmonte, M. K. Nazeeruddin, *Energy Environ. Sci.* **2018**, *11*, 952.

[16] a) J. Hu, I. W. H. Oswald, H. Hu, S. J. Stuard, M. M. Nahid, L. Yan, Z. Chen, H. Ade, J. R. Neilson, W. You, *ACS Mater. Lett.* **2019**, *1*, 171; b) J. Y. Ye, J. Tong, J. Hu, C. Xiao, H. Lu, S. P. Dunfield, D. H. Kim, X. Chen, B. W. Larson, J. Hao, K. Wang, Q. Zhao, Z. Chen, H. Hu, W. You, J. J. Berry, F. Zhang, K. Zhu, *Sol. RRL* **2020**, *4*, 2000082; c) Y. Cho, A. M. Soufiani, J. S. Yun, J. Kim, D. S. Lee, J. Seidel, X. Deng, M. A. Green, S. Huang, A. W. Y. Ho-Baillie, *Adv. Energy Mater.* **2018**, *8*, 1703392; d) D. S. Lee, J. S. Yun, J. Kim, A. M. Soufiani, S. Chen, Y. Cho, X. Deng, J. Seidel, S. Lim, S. Huang, A. W. Y. Ho-Baillie, *ACS Energy Lett.* **2018**, *3*, 647; e) T. Niu, J. Lu, M.-C. Tang, D. Barrit, D.-M. Smilgies, Z. Yang, J. Li, Y. Fan, T. Luo, I. McCulloch, A. Amassian, S. Liu, K. Zhao, *Energy Environ. Sci.* **2018**, *11*, 3358; f) S. Gharibzadeh, B. Abdollahi Nejand, M. Jakoby, T. Abzieher, D. Hauschild, S. Moghadamzadeh, J. A. Schwenzer, P. Brenner, R. Schmager, A. A. Haghighirad, L. Weinhardt, U. Lemmer, B. S. Richards, I. A. Howard, U. W. Paetzold, *Adv. Energy Mater.* **2019**, *9*, 1803699; g) Y. Zhang, G. Grancini, Z. F. Fei, E. Shirzadi, X. H. Liu, E. Oveisi, F. F. Tirani, R. Scopelliti, Y. Q. Feng, M. K. Nazeeruddin, P. J. Dyson, *Nano Energy* **2019**, *58*, 105; h) X. Jiang, J. Zhang, S. Ahmad, D. Tu, X. Liu, G. Jia, X. Guo, C. Li, *Nano Energy* **2020**, *75*, 104892; i) L. Liang, H. Luo, J. Hu, H. Li, P. Gao, *Adv. Energy Mater.* **2020**, *10*, 2000197.

[17] a) E. H. Jung, N. J. Jeon, E. Y. Park, C. S. Moon, T. J. Shin, T. Y. Yang, J. H. Noh, J. Seo, *Nature* **2019**, *567*, 511; b) J. Hu, I. W. H. Oswald, S. J. Stuard, M. M. Nahid, N. H. Zhou, O. F. Williams, Z. K. Guo,

L. Yan, H. M. Hu, Z. Chen, X. Xiao, Y. Lin, Z. B. Yang, J. S. Huang, A. M. Moran, H. Ade, J. R. Neilson, W. You, *Nat. Commun.* **2019**, *10*, 1276.

[18] M. Kepenekian, B. Traore, J. C. Blancon, L. Pedesseau, H. Tsai, W. Y. Nie, C. C. Stoumpos, M. G. Kanatzidis, J. Even, A. D. Mohite, S. Tretiak, C. Katan, *Nano Lett.* **2018**, *18*, 5603.

[19] F. X. Xie, C. C. Chen, Y. Z. Wu, X. Li, M. L. Cai, X. Liu, X. D. Yang, L. Y. Han, *Energy Environ. Sci.* **2017**, *10*, 1942.

[20] T. W. Jones, A. Osherov, M. Alsari, M. Sponseller, B. C. Duck, Y. K. Jung, C. Settens, F. Niroui, R. Brenes, C. V. Stan, Y. Li, M. Abdi-Jalebi, N. Tamura, J. E. Macdonald, M. Burghammer, R. H. Friend, V. Bulovic, A. Walsh, G. J. Wilson, S. Lilliu, S. D. Stranks, *Energy Environ. Sci.* **2019**, *12*, 596.

[21] a) S. Jariwala, H. Y. Sun, G. W. P. Adhyaksa, A. Lof, L. A. Muscarella, B. Ehrler, E. C. Garnett, D. S. Ginger, *Joule* **2019**, *3*, 3048; b) M. Kim, G. H. Kim, T. K. Lee, I. W. Choi, H. W. Choi, Y. Jo, Y. J. Yoon, J. W. Kim, J. Lee, D. Huh, H. Lee, S. K. Kwak, J. Y. Kim, D. S. Kim, *Joule* **2019**, *3*, 2179.

[22] J. T. W. Wang, Z. P. Wang, S. Pathak, W. Zhang, D. W. deQuilettes, F. Wisnivesky-Rocca-Rivarola, J. Huang, P. K. Nayak, J. B. Patel, H. A. M. Yusof, Y. Vaynzof, R. Zhu, I. Ramirez, J. Zhang, C. Ducati, C. Grovenor, M. B. Johnston, D. S. Ginger, R. J. Nicholas, H. J. Snaith, *Energy Environ. Sci.* **2016**, *9*, 2892.

[23] a) X. J. Zheng, C. C. Wu, S. K. Jha, Z. Li, K. Zhu, S. Priya, *ACS Energy Lett.* **2016**, *1*, 1014; b) W. S. Yang, B. W. Park, E. H. Jung, N. J. Jeon, Y. C. Kim, D. U. Lee, S. S. Shin, J. Seo, E. K. Kim, J. H. Noh, S. I. Seok, *Science* **2017**, *356*, 1376; c) Y. Y. Zhou, Y. X. Zhao, *Energy Environ. Sci.* **2019**, *12*, 1495.

[24] a) S. Lee, I. N. Ivanov, J. K. Keum, H. N. Lee, *Sci. Rep.* **2016**, *6*, 38168; b) D. Oka, T. Fukumura, *CrystEngComm* **2017**, *19*, 2144.

[25] a) I. J. Bae, O. C. Standard, G. J. Roger, D. Brazil, *J. Mater. Sci.: Mater. Med.* **2004**, *15*, 959; b) J. L. Mcardle, G. L. Messing, *J. Am. Ceram. Soc.* **1993**, *76*, 214.

[26] a) D. W. Ma, Z. S. Xu, F. J. Wang, X. J. Deng, *CrystEngComm* **2019**, *21*, 1458; b) J. M. Hoffman, X. Y. Che, S. Sidhik, X. T. Li, I. Hadar, J. C. Blancon, H. Yarnaguchi, M. Kepenekian, C. Katan, J. Even, C. C. Stoumpos, A. D. Mohite, M. G. Kanatzidis, *J. Am. Chem. Soc.* **2019**, *141*, 10661.

[27] M. E. Kamminga, H. H. Fang, M. R. Filip, F. Giustino, J. Baas, G. R. Blake, M. A. Loi, T. T. M. Palstra, *Chem. Mater.* **2016**, *28*, 4554.

[28] L. Gan, J. Li, Z. S. Fang, H. P. He, Z. Z. Ye, *J. Phys. Chem. Lett.* **2017**, *8*, 5177.

[29] A. Lemmerer, D. G. Billing, *CrystEngComm* **2010**, *12*, 4444.

[30] S. Prathapani, D. Choudhary, S. Mallick, P. Bhargava, A. Yella, *CrystEngComm* **2017**, *19*, 3834.

[31] T. Chen, B. J. Foley, C. Park, C. M. Brown, L. W. Harriger, J. Lee, J. Ruff, M. Yoon, J. J. Choi, S. H. Lee, *Sci. Adv.* **2016**, *2*, 1601650.

[32] D. W. deQuilettes, S. M. Vorpahl, S. D. Stranks, H. Nagaoka, G. E. Eperon, M. E. Ziffer, H. J. Snaith, D. S. Ginger, *Science* **2015**, *348*, 683.

[33] a) D. Y. Son, J. W. Lee, Y. J. Choi, I. H. Jang, S. Lee, P. J. Yoo, H. Shin, N. Ahn, M. Choi, D. Kim, N. G. Park, *Nat. Energy* **2016**, *1*, 16081; b) S. Ham, Y. J. Choi, J. W. Lee, N. G. Park, D. Kim, *J. Phys. Chem. C* **2017**, *121*, 3143.

[34] X. X. Shai, J. S. Wang, P. Y. Sun, W. C. Huang, P. Z. Liao, F. Cheng, B. W. Zhu, S. Y. Chang, E. P. Yao, Y. Shen, L. Miao, Y. Yang, M. K. Wang, *Nano Energy* **2018**, *48*, 117.

[35] D. Yang, R. X. Yang, K. Wang, C. C. Wu, X. J. Zhu, J. S. Feng, X. D. Ren, G. J. Fang, S. Priya, S. Z. Liu, *Nat. Commun.* **2018**, *9*, 3239.

[36] S. Zufle, S. Altazin, A. Hofmann, L. Jager, M. T. Neukom, W. Brutting, B. Ruhstaller, *J. Appl. Phys.* **2017**, *122*, 115502.

[37] Q. W. Han, J. Ding, Y. S. Bai, T. Y. Li, J. Y. Ma, Y. X. Chen, Y. H. Zhou, J. Liu, Q. Q. Ge, J. Chen, J. T. Glass, M. J. Therien, J. Liu, D. B. Mitzi, J. S. Hu, *Chem* **2018**, *4*, 2405.